Check for updates

PHYSICS

Pseudo-heterostructure and condensation of 1D moiré excitons in twisted phosphorene bilayers

Hongli Guo, Xu Zhang, Gang Lu*

Heterostructures are not expected to form in a single homogeneous material. Here, we show that planar pseudo-heterostructures could emerge in a twisted bilayer of phosphorene (tbP), driving in-plane energy and charge transfer. The formation of moiré superlattices combined with electronic anisotropy in tbPs yields one-dimensional (1D) moiré excitons with long radiative and nonradiative lifetimes, large binding energies, and deep moiré potentials. Low-frequency moiré phonons and dynamic moiré potentials are revealed to be responsible for the in-plane energy/charge transfer and exciton dynamics. The 1D moiré excitons are predicted to exhibit Bose-Einstein condensation at high temperatures and may lead to exotic Tonks-Girardeau Bose gases.

Copyright © 2023 The Authors, some rights reserved; exclusive licensee American Association for the Advancement of Science. No claim to original U.S. Government Works. Distributed under a Creative Commons Attribution NonCommercial License 4.0 (CC BY-NC).

INTRODUCTION

A heterostructure is an interface between two layers/regions of dissimilar semiconductors with distinct band structures. Heterostructures are at the heart of many modern technologies, including transistors, lasers, solar cells, etc. (*1*). Different types (I, II, and III) of band alignment (*2*) can arise in a heterojunction, providing a driving force for directed charge and energy transfer. However, such a band alignment or a heterostructure is not expected to appear in a single homogeneous material. Here, we show that planar pseudo-heterostructures could be formed in a twisted bilayer of phosphorene (tbP). On the basis of first-principles simulations, we predict that transient type I and type II band alignments could emerge in a tbP, driving in-plane energy and charge transfer. The planar heterostructures can host one-dimensional (1D) moiré excitons that could exhibit Bose-Einstein condensation (BEC) at high temperatures. The dynamics of the moiré excitons and the in-plane energy/charge transfer are attributed to low-frequency moiré phonons. Last, we propose that tbPs could potentially realize Tonks-Girardeau Bose gases (*3*), a long sought-after goal in atomic physics.

RESULTS

Since its discovery, 2D phosphorene has attracted substantial interest due to its tunable direct bandgap (*4*–*6*), high carrier mobility (*4*, *7*), and anisotropic electronic properties (*7*–*10*). Here, we focus on twisted bilayers of phosphorene in which periodic moiré superlattices are formed. In Fig. 1A, we display the moiré superlattice in a tbP with the twist angle θ = 2.6°. The unit cell of the moiré superlattice contains 2116 atoms and is indicated by a black box with a dimension of 73.06 and 55.44 Å in the zigzag (*x*) and armchair (*y*) directions, respectively. The moiré superlattice is composed of alternating strips of atomic layers, which are labeled as symmetric (S) or antisymmetric (AS) for the reason explained below. Each S (AS) strip consists of high-symmetry stacking motifs of Ta and Tb (Tc and Td), following the notation in (*11*); these motifs largely determine the moiré potential of the tbP.

Department of Physics and Astronomy, California State University Northridge, Northridge, CA 91330-8268, USA.
*Corresponding author. Email: ganglu@csun.edu

In Fig. 1 (B and C), we display the wave functions of the valence band maximum (VBM) and the conduction band minimum (CBM) for each stacking motif, respectively. It is found that the VBM wave function is even for Ta and Tb but odd for Tc and Td, relative to the inversion center (red cross). For this reason, the strip with Ta and Tb motifs is designated as S, while the strip with Tc and Td motifs is designated as AS. The CBM wave function, on the other hand, is even for all four stacking motifs. Since the VBM and CBM wave functions have the same even (+) parity in strip S, the corresponding transition dipole (from VBM to CBM) should vanish (*12*). Therefore, the lowest exciton in the S strip must be dark, whereas the AS strip could host bright excitons.

In the following, we perform time-dependent density functional theory (TDDFT) calculations with optimally tuned, screened, and range-separated hybrid (OT-SRSH) functionals to determine the oscillator strengths of low-energy excitons in three tbPs (θ = 2.6°, 5.3°, and 7.0°). The information of each moiré superlattice is summarized in table S1. As shown in Fig. 2A, three low-energy excitons are considered: (i) D is the lowest exciton in these bilayers, and its charge density is shown in Fig. 2B. Although D is a dark exciton, its electron and hole have a strong spatial overlap, and both are localized in the S layer, forming an array of optically dark strips in the tbP. (ii) B is a bright exciton with its electron and hole localized in the AS layer, forming another array of optically active strips. (iii) I is a charge-transfer exciton whose electron and hole are separated across the unit cell. Both exciton B and D have a large binding energy, 0.51 and 0.44 eV, respectively. Exciton I, on the other hand, has a much smaller binding energy of 0.09 eV.

For θ = 7.0°, all three excitons are energetically well separated, with exciton B reminiscent of a deep defect state. Hence, the twisted bilayer can be considered as a planar pseudo-heterostructure (*13*) with multiple S/AS heterojunctions. For a smaller twist angle (θ = 2.6° and 5.3°), the bilayer behaves as a type I heterostructure and under excitation, the bright B excitons would funnel from AS to S (i.e., energy transfer). For a larger twist angle (θ =7.0), the bilayer can be regarded as a type II heterostructure that enables charge transfer. When excited, the bright excitons B will decay to I with electron transfer from AS to S, and, similarly, the exciton I can decay to exciton D with hole transfer from AS to S. That is, spontaneous in-plane energy and charge transfer can be realized in the tbP. Recently, an interesting strategy is proposed to funnel

Downloaded from https://www.science.org on December 19, 2025

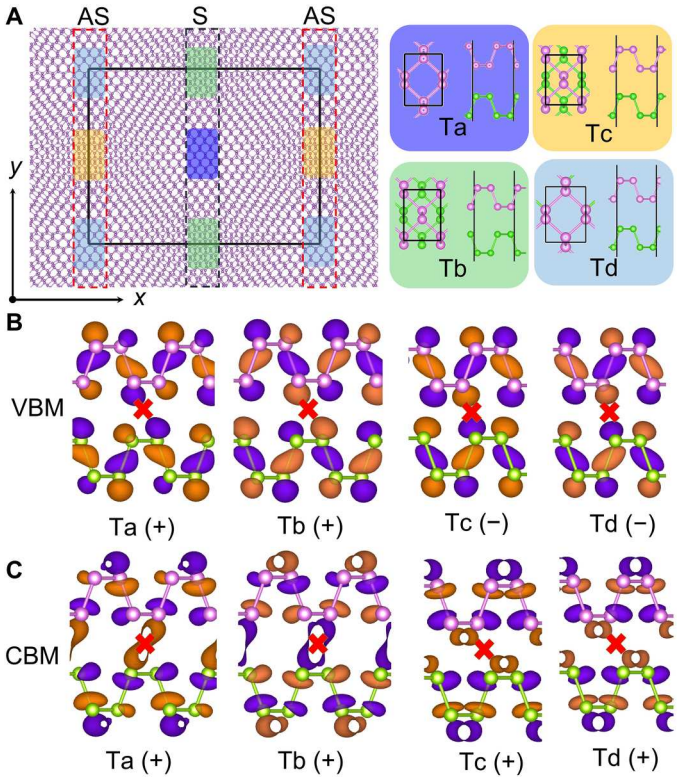

Fig. 1. Atomic structure and symmetry of wave functions of the tbP. (**A**) The moiré superlattice and its unit cell (black box) in the tbP (θ = 2.6°) with the S and AS strips outlined by the dashed box. Four stacking motifs (Ta, Tb, Tc, and Td) are highlighted with their atomic structures (top and side views) displayed on the right. The wave functions of the VBM (**B**) and CBM (**C**) for the four stacking motifs are displayed. The purple and brown isosurfaces indicate the positive and negative phases of the wave function, respectively. The red cross denotes the inversion center, and (+) and (−) signs indicate the even and odd parity, respectively.

or confine excitons and charge carriers in 2D semiconductors and nanowires via strain engineering (*13*, *14*). Essentially, a spatially varying distribution of the bandgap is created by mechanical strains to drive excitons and charge carriers. Here, the tbP is shown to produce a spatial variation of the bandgap in the absence of external stress, as illustrated in Fig. 2C. In particular, the bandgap distribution exhibits a 1D character with a large gradient along *x* direction, driving the in-plane energy and charge transfer. Note that the bandgap distribution in a moiré unit cell is also defined as the moiré potential (*15*, *16*) whose amplitude is 0.34 eV for the tbP.

Although the single-particle band structure is widely used to characterize energy and charge transfer in heterostructures, one should be wary of its limitation in 2D materials with a strong excitonic effect. For example, the bandgap distribution in Fig. 2C indicates that there exists an energy barrier separating AS and S in the *x* direction. However, the TDDFT calculations that include the excitonic effect suggest that the exciton can funnel spontaneously from AS to S. According to the electron-hole transition amplitude analysis (fig. S2), exciton D is mainly composed of an excitation from VBM − 2 to CBM, while exciton B is from VBM to CBM + 6, and exciton I is from VBM to CBM, as shown schematically in Fig. 2D. On the basis of the single-particle picture, one would expect that when exciton B is excited, its electron should fall from CBM + 6 to CBM, while its hole remains at VBM. Similarly, one would expect the energy of exciton I to be smaller than that of exciton D for θ = 7.0°. However, both expectations are contradictory to the TDDFT results. It turns out that the decreased electron energy (CBM + 6 ➔ CBM) overcompensates the increased hole energy (VBM ➔ VBM − 2), which drives the excitonic transition B ➔ D, due to the electron-hole interaction captured in the TDDFT calculation. In the same vein, exciton I has a higher energy than D because the former has a much smaller exciton binding energy owing to its well-separated electron-hole pair. The single-particle band structure is misleading here because it does not include the electron-hole interaction.

The emergence of the planar heterostructure in the tbP is attributed to the formation of the moiré superlattice and the anisotropy of its electronic structure. The former yields the spatial variation of the bandgap (i.e., the moiré potential) that provides band offsets for the pseudo-heterostructure and the in-plane energy and charge transfer. The latter, on the other hand, renders the moiré potential 1D and the heterostructure planar. In particular, the 1D distributions of the wave functions (fig. S3) result from anisotropic effective masses of charge carriers (*17*). In addition, exciton B is found to be linearly polarized (fig. S4), which is a hallmark of 1D moiré excitons (*18*, *19*). The presence of the 1D bright excitons in tbPs could lead to novel photonic and optoelectronic applications, such as low-pass waveguide filters and selective interconnections in planar photonic circuits (*20*). We should also point out the possibility of forming 0D heterostructures and moiré excitons in tbPs of small twist angles (θ < 2°) owing to the presence of 0D quantum dot–like states in these bilayers (*21*). The schematic diagram of 0D heterostructures can be found in fig. S5.

The properties of moiré excitons can be tuned by the twist angle. For example, as θ increases from 2.6° to 5.3° and 7.0°, the oscillator strength of the charge-transfer exciton I increases significantly, turning it from dark to bright (Fig. 2A). This is because as θ increases, the moiré lattice constant shrinks, and so does the electron-hole separation distance in exciton I. Hence, the electron and hole wave function overlap is enhanced to yield a much higher oscillator strength. For the same reason, the binding energy of exciton I is increased, while its transition energy redshifts as the angle increases (Fig. 2E). In contrast, the transition energy of exciton B and D both blueshifts with increasing θ, and their binding energies also increase. The oscillator strength and lifetime of B and D exciton can also be tuned by the twist angle as shown in Fig. 2 (A and F). In particular, we find that the radiative lifetime of exciton D at 300 K can vary by more than one order of magnitude as θ changes from 2.6° to 7.0°. As shown in fig. S6, one can also tune the oscillator strength and energy of the moiré excitons by an out-of-plane electric field. Thus, similar to conventional heterostructures, the pseudo-heterostructure is highly tunable to be used in device applications.

Next, we examine the lifetime of moiré excitons in tbPs, including the radiative and nonradiative contributions. While the radiative lifetime can be readily derived from the oscillator strength of the exciton, the nonradiative lifetime is much more difficult to calculate. In this work, we determine the nonradiative lifetime of the moiré excitons based on an approach that combines nonadiabatic molecular dynamics (NAMD) with the TDDFT-OT-SRSH method (*22*) so that the exciton-phonon coupling is captured

Downloaded from https://www.science.org on December 19, 2025

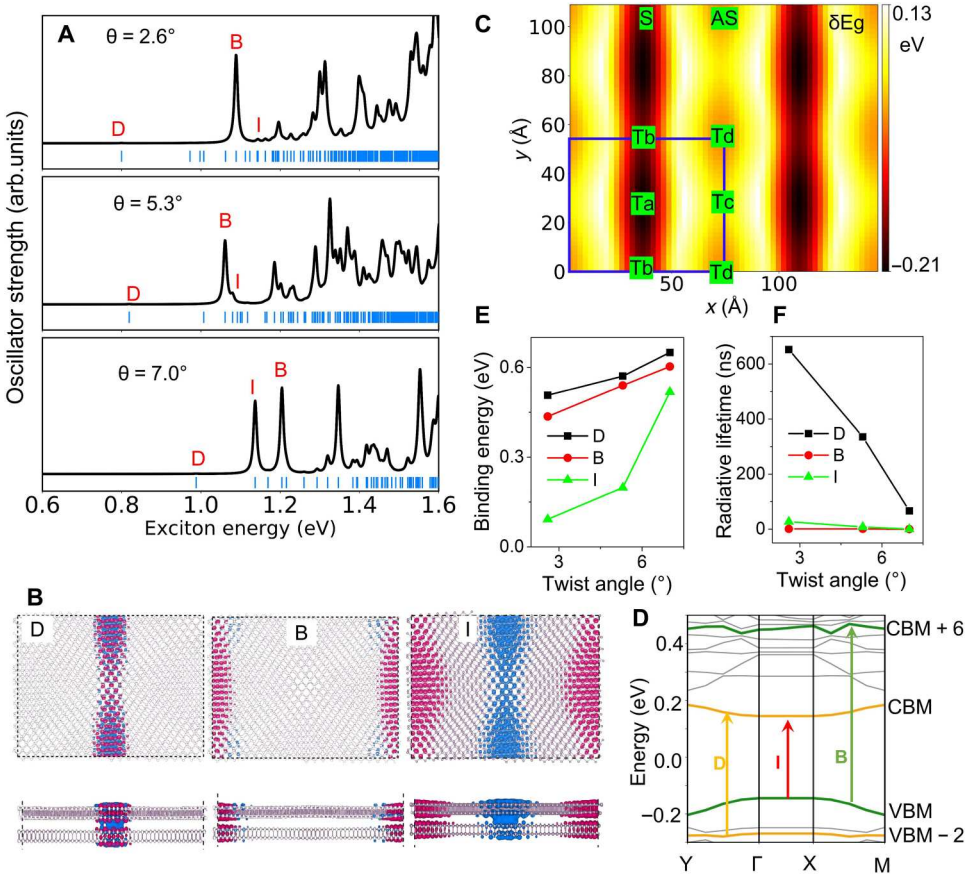

Fig. 2. 1D moiré excitons and moiré potential. (**A**) The exciton oscillator strength in three tbPs (θ = 2.6°, 5.3°, and 7.0°) with the blue bars representing the exciton energy levels. (**B**) Top and side views of the exciton (D, B, and I) charge density in the superlattice unit cell (dashed box) for θ = 2.6°. The blue and red colors represent the electron and hole charge density, respectively. All isosurface values are set at 0.0001 e/Å^3. (**C**) The spatial variation of the bandgap (δE_g) in the moiré superlattice (θ = 2.6°). The moiré unit cell (blue box) and the stacking motifs are indicated. (**D**) The single-particle band structure for the tbP (θ = 2.6°) with the corresponding excitations for excitons D, B, and I. (**E**) Twist angle dependence of the binding energy for B, D, and I excitons. (**F**) Twist angle dependence of the radiative lifetime for B, D, and I excitons at 300 K.

(details can be found in Materials and Methods). The radiative lifetime for exciton D in the tbP (θ = 7.0°) is estimated as 66.3 ns at 300 K. The nonadiabatic evolution or decay dynamics of exciton D is shown in Fig. 3A from which one can derive its nonradiative lifetime (9.8 ns). The nonradiative lifetime is shorter than the radiative lifetime but longer than the nonradiative lifetime (1.2 ns) of the lowest exciton in the nontwisted phosphorene bilayer owing to the momentum mismatch in the twisted bilayer. The overall lifetime τ of exciton D is estimated as 8.5 ns using the expression $\frac{1}{\tau} = \frac{1}{\tau_{\text{radiative}}} + \frac{1}{\tau_{\text{nonradiative}}}$. In addition, we have examined phonon-assisted decay of exciton B to excitons I and D as shown in Fig. 3B. The in-plane energy (blue) and charge (green) transfer takes place simultaneously, driven by the transient pseudo-heterostructure; the estimated transfer time is about 580 fs. This decay/transfer time is much longer than the typical energy/charge transfer time in transition metal dichalcogenide (TMD) heterostructures partly because the in-plane distance of the S/AS heterojunction is ~2 nm, much larger than the interlayer distance (3 to 4 Å) in TMD bilayers. We can also estimate the thermalization time scale of exciton D by a Fourier transformation (FT) of its time-dependent energy as shown in Fig. 3C; for comparison, we have also included the FT spectrum for the lowest exciton in the nontwisted bilayer. The high-frequency peaks in 250 to 450 cm^{-1} range correspond to intralayer A_g^1, B_{2g}, and A_g^2 phonon modes (*23*, *24*). The low-frequency 25 cm^{-1} phonon is the interlayer shear mode, and the additional phonon near 80 cm^{-1} is the interlayer breathing mode. The moiré phonons in the twisted bilayer have slightly smaller frequencies than the corresponding modes in the nontwisted bilayer. The interlayer shear modes around ~25 cm^{-1} yield the highest intensity and, thus, are most strongly coupled to the exciton dynamics. That is, these phonons are responsible for exciton thermalization whose time scale is estimated as ~13 ps, much shorter than the lifetime of exciton D. In Fig. 3D, we display the charge density of exciton D at selective snapshots (280, 1160, 2025, and 3874 fs) in the NAMD simulation. We find that the exciton remains localized in S layer, which is itself dynamical, i.e., the lattice vibration could shift the positions of the stacking motifs. In particular, the location of motif Td changes at different snapshots. That is, there is a connection between the dynamics of moiré excitons and moiré potentials, which could lead to interesting phenomena. For example, since the low-frequency shear modes can be populated at low temperatures, they could lead to translations of the moiré potential, thus

Downloaded from https://www.science.org on December 19, 2025

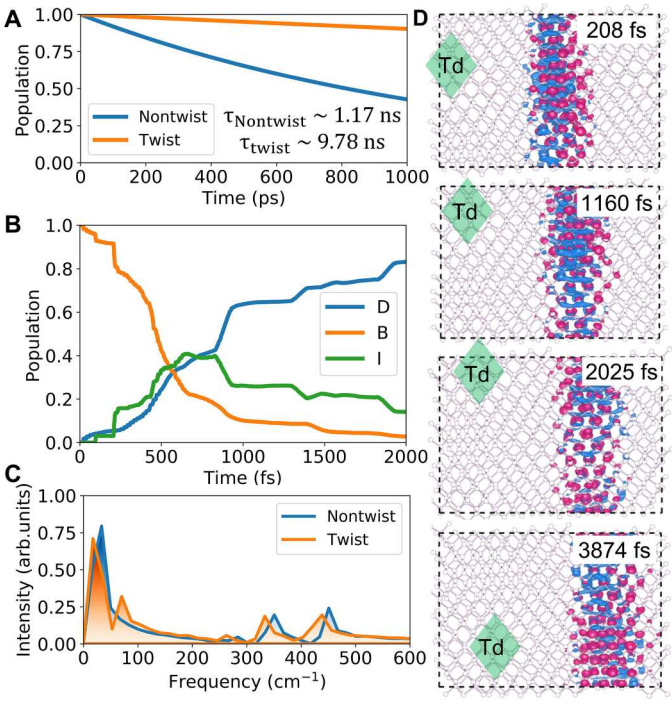

Fig. 3. Dynamics of moiré excitons. (**A**) The evolution (or decay) dynamics of the lowest exciton in the nontwisted (blue) and twisted phosphorene bilayer (orange) (θ = 7.0°). (**B**) The nonadiabatic evolution of exciton B, D, and I in the tbP (θ = 7.0°) with exciton B as the initial state; the crossing point is at ~580 fs. (**C**) The FT spectra for the time evolution of D exciton in the tbP (θ = 7.0°) and of the lowest exciton in the nontwisted bilayer. (**D**) The charge density of exciton D at different NAMD snapshots with the location of motif Td indicated. Blue and red colors represent the charge density of the electron and the hole, respectively. All isosurface values are set at 0.0001 e/Å^3.

diffusion of moiré excitons trapped at the potential. This could explain anomalous exciton diffusion at low temperatures in moiré heterostructures (*25*).

BEC of excitons is of great scientific interest because it can occur at a much higher temperature than atomic gases, due to much lighter masses of excitons. It has been recognized that semiconductor bilayers with strong exciton binding could be ideal systems to realize high-temperature exciton condensation (*26*, *27*). Recently, several theoretical studies have predicted that the BEC temperature could reach ~100 K in 2D van der Waals (vdW) heterostructures (*28*–*30*), and experimental evidence for high-temperature exciton condensation has been reported in TMD bilayers (*31*). In the previous works, the ground-state wave functions of the excitons are 2D. Here, we are interested in BEC of quasi-1D excitons that has not been reported before. In addition, we propose that tbPs could offer a tunable solid-state platform to explore Tonks-Girardeau gases, which are of particular interest in atomic physics (*32*, *33*).

The excitonic BEC transition temperature T_c depends on several key factors: (i) The excitons should have longer lifetimes than their thermalization times (*34*). (ii) The exciton binding energy should be large enough, typically >10$k_B T_c$ (k_B is Boltzmann constant) (*28*, *35*). (iii) The presence of potential traps that confine the exciton condensate. As shown in Fig. 2A, the ground state of the condensate, i.e., exciton D, is well separated in energy from other excitons. The lifetime of exciton D is estimated as 8.5 ns, which is ~3 orders of magnitude longer than its thermalization time (~13 ps), thus meeting the first requirement. The binding energy of exciton D is estimated as 0.44 eV, which could lead to T_c ~ 300 to 400 K according to the second requirement. Last, the presence of moiré potentials in the tbPs could provide deep traps for the exciton condensate. As shown in Fig. 2C, the amplitude of the moiré potential could reach ~0.34 eV. Here, we follow an earlier work (*36*, *37*) to estimate the BEC temperature T_c (details can be found in Materials and Methods). For the tbP (θ = 2.6°), we can determine the Bohr radius and effective mass of exciton D as well as the moiré potential from the first-principles calculations. We can then calculate T_c as a function of λ that is the strength of repulsive exciton-exciton interaction. As shown in Fig. 4, when λ = 0, the corresponding T_c is estimated as 385 K, which is much higher than the BEC temperature reported in TMD bilayers (100 to 150 K). The higher T_c in the tbP is mainly due to a smaller effective mass of exciton D, which, in turn, arises from its 1D nature (high mobility in the y direction). The presence of strongly bound 1D excitons trapped by moiré potentials implies that these 1D excitons could become Tonks-Girardeau gases (*3*, *32*, *33*) that behave similar to noninteracting fermions ("fermionization" of bosons) in a strong interaction regime (with a large λ). The inter-exciton distance, hence, the interaction strength λ can be tuned by the twist angle. The ability to probe Tonks-Girardeau gases in a tunable solid-state system could have a major impact on atomic and many-body physics.

DISCUSSION

In summary, by means of first-principles calculations, we show that planar pseudo-heterostructures could emerge in tbPs because of the spatial distribution of the bandgap, which provides appropriate energy alignments for the in-plane energy and charge transfer. The presence of the moiré superlattices and the anisotropic electronic structure in tbPs yields tunable 1D moiré excitons and moiré potentials. The combination of long radiative and nonradiative lifetime, large binding energy, small effective mass, and deep moiré potential for the lowest moiré exciton leads to 1D BEC at high temperatures (300 to 400 K). The nonadiabatic dynamics of the moiré excitons is examined, which reveals dynamic nature of the moiré potential. The tbPs are envisioned to realize Tonks-Girardeau gases and waveguide filters and selective interconnections in planar photonic circuits.

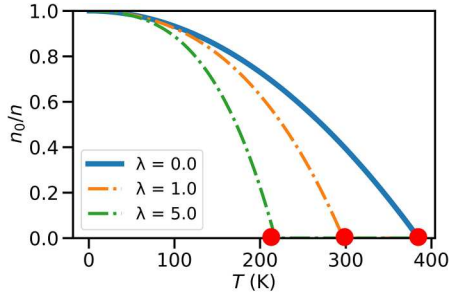

Fig. 4. 1D BEC of moiré exciton. The condensation fraction n_0/n as a function of temperature T with the total exciton density $n = 2.6 \times 10^{12}$ cm^{-2}; each curve corresponds to a different interaction strength λ. The BEC transition temperature T_c is indicated by the red dot with the condensed exciton density $n_0 = 0$.

Downloaded from https://www.science.org on December 19, 2025

MATERIALS AND METHODS

First-principles ground-state calculations

The ground-state properties, including single-particle band structures and optimized atomic structures of various bilayers examined in this work, were determined using Vienna Ab initio Simulation Package (*38*, *39*). The Perdew-Burke-Ernzerhof exchange-correlation functional (*40*) along with projector-augmented wave potentials (*41*) was used in these calculations. The vdW interaction was considered via vdW-D2 functional (*42*). The atomic geometry in each moiré superlattice was fully optimized until the residual force on each atom was less than 0.01 eV/Å. A 20 Å vacuum layer was included in the supercell to separate the periodic images. The structural reconstruction for the moiré supercell (θ = 2.6°) is shown in fig. S7. To determine the band structures of the tbP moiré superlattices, five special *k*-points were sampled along each of the high symmetry directions in the Brillouin zone. To calculate the spatial variation of the bandgap, we define a displacement vector **d** between a pair of nearest-neighbor atoms across the interface in the unit cell of a nontwisted phosphorene bilayer, shown in fig. S8. We then deform the bilayer by introducing a relative shift **d** between the two layers and calculate the bandgap of the nontwisted phosphorene bilayer as a function of **d**. Last, we determine **d** for each atom in a twisted bilayer after the structural relaxation. From **d**, we can find the bandgap at each atom of the twisted bilayer.

First-principles excited-state calculations

To determine the energies and the many-body wave functions of the excitons in the bilayers, we used a recently developed first-principles approach based on the linear-response TDDFT (LR-TDDFT) (*43*, *44*) with OT-SRSH exchange-correlation functionals (*15*, *18*, *45*–*48*). Unlike traditional LR-TDDFT method with local and semilocal functionals, the TDDFT method using the OT-SRSH functionals can capture the correct long-range electron-electron and electron-hole interactions in solids by choosing appropriate parameters (*49*–*53*). The LR-TDDFT methods with hybrid exchange-correlation functionals have been used extensively to study optical and excitonic properties in solids, see, for example, (*54*–*56*) and references therein, in addition to (*49*–*53*). In this work, we solve the following non-Hermitian eigenvalue equations of Casida (*57*) to determine the excitation energies ω_I

$$\begin{pmatrix} \mathbf{A} & \mathbf{B} \\ \mathbf{B}^* & \mathbf{A}^* \end{pmatrix} \begin{pmatrix} X_I \\ Y_I \end{pmatrix} = \omega_I \begin{pmatrix} 1 & 0 \\ 0 & -1 \end{pmatrix} \begin{pmatrix} X_I \\ Y_I \end{pmatrix} \quad (1)$$

where the pseudo-eigenvalue ω_I is the *I*th exciton energy level and $X_{I,ij}$ and $Y_{I,ij}$ are eigenvectors that are used to determine the exciton wave functions. The matrix elements of **A** and **B** in the basis of Kohn-Sham (KS) orbitals ($ij\sigma$) are given by

$$A_{ij\sigma,kl\tau} = \delta_{i,k}\delta_{j,l}\delta_{\sigma,\tau}(\varepsilon_{j\sigma} - \varepsilon_{i\sigma}) + K_{ij\sigma,kl\tau} \quad (2)$$

$$B_{ij\sigma,kl\tau} = K_{ij\sigma,lk\tau} \quad (3)$$

Here, $K_{ij\sigma,lk\tau}$ is the coupling matrix whose indices *i* and *k* indicate the occupied KS orbitals and *j* and *l* represent the virtual KS orbitals (*58*). Following the assignment ansatz of Casida (*57*), the many-body wave function of the excited state *I* can be written as

$$\Phi_I \approx \sum_{ij\sigma} \frac{\mathbf{X}_{I,ij\sigma} + \mathbf{Y}_{I,ij\sigma}}{\sqrt{\omega_I}} a^\dagger{}_{j\sigma} a_{i\sigma} \Phi_0 = \sum_{ij\sigma} Z_{I,ij} a^\dagger{}_{j\sigma} a_{i\sigma} \Phi_0 \quad (4)$$

where $z_{I,ij} = (\mathbf{X}_{I,ij} + \mathbf{Y}_{I,ij})/\sqrt{\omega_I}$. $a_{i\sigma}$ ($a^\dagger_{i\sigma}$) is the annihilation (creation) operator acting on the *i*th KS orbital with spin σ and Φ_0 is the ground-state many-body wave function taken as the single Slater determinant of the occupied KS orbitals.

In the (TD)DFT-OT-SRSH method, there are three parameters, α, β, and γ, needed to be specified. α controls the short-range exact exchange, and β is chosen to satisfy the requirement α + β = 1/ε, where ε is the scalar dielectric constant. The optimal set of the parameters (α = 0.1203, β =0.7130, and γ = 0.0655) was determined by fitting the quasiparticle gap of the nontwisted black phosphorene (BP) bilayer from the DFT-OT-SRSH calculations to that from the GW calculations. With this set of parameters, we obtained an optical gap of 0.98 eV and a quasiparticle gap of 1.58 eV for the nontwisted BP bilayer, respectively, which agrees well to the previous GW-Bethe–Salpeter (GW-BSE) calculation (*10*). The exciton binding energy E_b defined as the difference between the quasiparticle gap and the optical gap is calculated as 0.60 eV, which is also in line with the previous GW-BSE calculation (*10*, *59*). To further validate our method, we compute the exciton charge density and the electronic part of the excitonic wave function for the lowest exciton in the nontwisted bilayer BP. The results shown in fig. S1 are in good agreement with the GW-BSE calculation (*59*). As very large supercells are used in the TDDFT calculations for the moiré excitons, only Γ point of the Brillouin zone is sampled.

Polarization-dependent oscillator strength and radiative lifetime

To determine the optical dipole moment for each moiré exciton, we first examine electron-hole transitions involved in the exciton. As mentioned above, the many-body wave function of the exciton Φ_I is expressed as a linear combination of electron-hole transitions, and $Z_{I,ij}$ represents the corresponding electron-hole transition amplitude. The polarization-dependent optical dipole moment (μ_I) of the exciton *I* is calculated as

$$\mu_I = \sum_{ij} Z_{I,ij} p_{ij} \quad (5)$$

$$p_{ij} = \langle \varphi_i | \hat{\varepsilon} \cdot \mathbf{r} | \varphi_j \rangle \quad (6)$$

where p_{ij} is the transition dipole moment between the KS occupied state ϕ_i and unoccupied state ϕ_j. $\hat{\varepsilon}$ is the unit vector of the electric field of the polarized light, and **r** is the position operator of the electron. The oscillator strength is then determined by

$$f = \frac{2\omega_I}{\hbar} * {\mu_I}^2 \quad (7)$$

where ω_I is the exciton energy. The radiative recombination rate of an exciton is given by (*60*)

$$\gamma_I = \frac{e^2 \omega_I {\mu_I}^2}{\varepsilon_0 \hbar^2 c A_{uc}} \quad (8)$$

Here, A_{uc} is the area of the in-plane unit cell, *e* is the electron charge, ε_0 is the vacuum permittivity, and *c* is the speed of light.

Downloaded from https://www.science.org on December 19, 2025

The radiative lifetime of the exciton at 0 K is given as

$$\tau_0 = {\gamma_I}^{-1} \quad (9)$$

The radiative lifetime of the exciton at a finite temperature T is calculated as

$$\tau(T) = \tau_0 \left[\frac{3}{4}\left(\frac{2Mc^2 k_B T}{{\omega_I}^2}\right)\right] \quad (10)$$

where M is the exciton effective mass and k_B is Boltzmann constant.

Nonadiabatic molecular dynamics

After geometric optimization at 0 K, the system is heated to 300 K for 4 ps by velocity rescaling. Then, a 4 ps ab initio molecular dynamics (AIMD) trajectory is obtained in the microcanonical ensemble with a 1 fs time step. At each AIMD time step, we perform TDDFT calculations to obtain the excited state properties (exciton energy, wave functions, etc.). In particular, the time-dependent many-body wave function of the exciton $\Psi(t)$ is expanded by a linear combination of a complete basis set consisted of the adiabatic ground state and the excited states $\Phi_I[\mathbf{R}(t)]$ at the present ionic positions $\mathbf{R}(t)$

$$\Psi(t) = \sum_{I=0}^{\infty} C_I(t)\Phi_I[\mathbf{R}(t)] \quad (11)$$

where $C_I(t)$ is the expansion coefficient. Let the initial exciton state start in a pure state I at $t = 0$ (i.e., $\Phi_I[\mathbf{R}(t)]$), and then the coefficient $C_J(t)$ in Eq. 11 can be labeled as $C_J^{(I)}(t)$ with the initial condition $C_J^{(I)}(0) = \delta_{I,J}$. At $t > 0$, ions move and $\Psi(t)$ becomes a mixed state. Therefore, $|C_J^{(I)}(t)|^2$ represents the probability that the excited state makes a transition from state I to state J during a time interval of t. The evolution of $C_J(t)$ can be determined from the NAMD at each time step. Substituting Eq. 11 into the time-dependent Schrödinger equation, one arrives at the following equation involving the expansion coefficient $C_J(t)$

$$\frac{\partial}{\partial t}C_J(t) = -\sum_K C_K(t)\left(\frac{i}{\hbar}\omega_K\delta_{JK} + D_{JK}\right) \quad (12)$$

A standard second-order finite-difference method with a time step of 10^{-3} fs is used to propagate the coefficient $C_J(t)$. In addition, D_{JK} is the nonadiabatic coupling between two many-body electronic states J and K

$$D_{JK} \equiv \langle\Phi_J|\nabla_R|\Phi_K\rangle \cdot \frac{dR}{dt} = \langle\Phi_J|\frac{\partial}{\partial t}|\Phi_K\rangle \quad (13)$$

Substituting Eq. 4 into Eq. 13, we can obtain D_{JK} as

$$\begin{aligned} D_{JK} &= \sum_{ii',jj'} Z^*_{J,ij} Z_{K,i'j'} \langle\Phi_{ij}|\frac{\partial}{\partial t}|\Phi_{i'j'}\rangle \\ &= \sum_{i,j\neq j'} Z^*_{J,ij} Z_{K,ij'} d_{jj'} - \sum_{i\neq i',j} Z^*_{J,ij} Z_{K,i'j} d_{ii'} \end{aligned} \quad (14)$$

where $\Phi_{ij} = \hat{a}_j^\dagger \hat{a}_i \Phi_0$ is a single Slater determinant of the KS orbitals, promoting an electron from an occupied state i to a virtual state j. $d_{jk} = \langle\phi_j|\frac{\partial}{\partial t}|\phi_k\rangle$ is the nonadiabatic coupling between the KS orbitals. The nonadiabatic coupling between the excited state J and the ground state is obtained as

$$D_{J0} = \sum_{i,j} Z^*_{J,ij} d_{ji} \quad (15)$$

Last, we used fewest switches surface hopping NAMD (*61*–*63*) to simulate the nonradiative exciton dynamics. To simulate exciton dynamics on a nanosecond time scale, the 4 ps nonadiabatic Hamiltonian is iterated 250 times, similar to previous works (*64*–*66*).

BEC transition temperature

Following the approach in (*36*, *37*), the moiré excitons in the tbP can be regarded as a Bose gas trapped in a 1D harmonic oscillator potential. When the exciton-exciton interaction is ignored, BEC transition temperature can be estimated as

$${T_c}^0 = \left(\frac{3h^3 n}{\sqrt{2}{k_B}^2\pi^4 M^{3/2}}\right)^{1/2} \kappa^{1/4} \quad (16)$$

where h is the Plank constant and n is the exciton density. The critical exciton density is given by $n_c = 1/(\pi R^2)$, where R is the exciton Bohr radius that can be estimated by the root mean square radius of the exciton wave function (*30*). R is determined to be 3.5 nm, and the critical exciton density is $n_c = 2.6 \times 10^{12}\text{cm}^{-2}$. M is the exciton effective mass along the direction of the trap potential and is estimated as 0.45 m_0 by adding up the effective masses of the electron and hole. κ is the coefficient for the confining potential defined as $U = \kappa y^2$. As the 1D confining potential is along the y direction, U is estimated as 0.1 eV by calculating the gap variation in the S strip along the y direction shown in Fig. 2C. Last, ${T_c}^0$ is determined to be 385 K. The condensation fraction as a function of temperature T is defined by

$$n_0/n = 1 - \left(\frac{T}{T_c^0}\right)^2 - \lambda\left(\frac{T}{T_c^0}\right)^{7/2} \quad (17)$$

where n_0 is the condensed exciton density and T_c^0 is T_c when $\lambda = 0$. λ is the repulsive exciton-exciton interaction strength, given by the ratio between the interaction energy and the thermal kinetic energy of the exciton gas. When the exciton-exciton interaction is considered, the transition temperature T_c is determined by Eq. 16 when $n_0 = 0$.

Supplementary Materials

This PDF file includes:

Figs. S1 to S8
Table S1

REFERENCES AND NOTES

1. Z. I. Alferov, Nobel lecture: The double heterostructure concept and its applications in physics, electronics, and technology. *Rev. Mod. Phys.* **73**, 767–782 (2001).
2. V. O. Özçelik, J. G. Azadani, C. Yang, S. J. Koester, T. Low, Band alignment of two-dimensional semiconductors for designing heterostructures with momentum space matching. *Phys. Rev. B* **94**, 035125 (2016).
3. D. S. Petrov, G. V. Shlyapnikov, J. T. M. Walraven, Regimes of quantum degeneracy in trapped 1D gases. *Phys. Rev. Lett.* **85**, 3745–3749 (2000).
4. J. Qiao, X. Kong, Z.-X. Hu, F. Yang, W. Ji, High-mobility transport anisotropy and linear dichroism in few-layer black phosphorus. *Nat. Commun.* **5**, 4475 (2014).
5. A. S. Rodin, A. Carvalho, A. H. Castro Neto, Strain-induced gap modification in black phosphorus. *Phys. Rev. Lett.* **112**, 176801 (2014).

Downloaded from https://www.science.org on December 19, 2025

6. Z. Zhang, L. Li, J. Horng, N. Z. Wang, F. Yang, Y. Yu, Y. Zhang, G. Chen, K. Watanabe, T. Taniguchi, X. H. Chen, F. Wang, Y. Zhang, Strain-modulated bandgap and piezo-resistive effect in black phosphorus field-effect transistors. *Nano Lett.* **17**, 6097–6103 (2017).
7. H. Liu, A. T. Neal, Z. Zhu, Z. Luo, X. Xu, D. Tománek, P. D. Ye, Phosphorene: An unexplored 2D semiconductor with a high hole mobility. *ACS Nano* **8**, 4033–4041 (2014).
8. T. Low, A. S. Rodin, A. Carvalho, Y. Jiang, H. Wang, F. Xia, A. H. Castro Neto, Tunable optical properties of multilayer black phosphorus thin films. *Phys. Rev. B* **90**, 075434 (2014).
9. F. Xia, H. Wang, J. C. M. Hwang, A. H. C. Neto, L. Yang, Black phosphorus and its isoelectronic materials. *Nat. Rev. Phys.* **1**, 306–317 (2019).
10. V. Tran, R. Soklaski, Y. Liang, L. Yang, Layer-controlled band gap and anisotropic excitons in few-layer black phosphorus. *Phys. Rev. B* **89**, 235319 (2014).
11. L.-y. Huang, X. Zhang, M. Zhang, G. Lu, Optically inactive defects in monolayer and bilayer phosphorene: A first-principles study. *Phys. Rev. Mater.* **2**, 054003 (2018).
12. Y. Peter, M. Cardona, *Fundamentals of Semiconductors: Physics and Materials Properties* (Springer Science & Business Media, 2010).
13. D. Nam, D. S. Sukhdeo, J.-H. Kang, J. Petykiewicz, J. H. Lee, W. S. Jung, J. Vũković, M. L. Brongersma, K. C. Saraswat, Strain-induced pseudoheterostructure nanowires confining carriers at room temperature with nanoscale-tunable band profiles. *Nano Lett.* **13**, 3118–3123 (2013).
14. J. Feng, X. Qian, C.-W. Huang, J. Li, Strain-engineered artificial atom as a broad-spectrum solar energy funnel. *Nat. Photon.* **6**, 866–872 (2012).
15. H. Guo, X. Zhang, G. Lu, Shedding light on moiré excitons: A first-principles perspective. *Sci. Adv.* **6**, eabc5638 (2020).
16. F. Wu, T. Lovorn, A. H. MacDonald, Topological exciton bands in Moiré heterojunctions. *Phys. Rev. Lett.* **118**, 147401 (2017).
17. P. Kang, W.-T. Zhang, V. Michaud-Rioux, X.-H. Kong, C. Hu, G.-H. Yu, H. Guo, Moiré impurities in twisted bilayer black phosphorus: Effects on the carrier mobility. *Phys. Rev. B* **96**, 195406 (2017).
18. S. Zhao, E. Wang, E. A. Üzer, S. Guo, R. Qi, J. Tan, K. Watanabe, T. Taniguchi, T. Nilges, P. Gao, Y. Zhang, H.-M. Cheng, B. Liu, X. Zou, F. Wang, Anisotropic moiré optical transitions in twisted monolayer/bilayer phosphorene heterostructures. *Nat. Commun.* **12**, 3947 (2021).
19. Y. Bai, L. Zhou, J. Wang, W. Wu, L. J. McGilly, D. Halbertal, C. F. B. Lo, F. Liu, J. Ardelean, P. Rivera, N. R. Finney, X.-C. Yang, D. N. Basov, W. Yao, X. Xu, J. Hone, A. N. Pasupathy, X.-Y. Zhu, Excitons in strain-induced one-dimensional moiré potentials at transition metal dichalcogenide heterojunctions. *Nat. Mater.* **19**, 1068–1073 (2020).
20. Y. Luan, H. Zobeiri, X. Wang, E. Sutter, P. Sutter, Z. Fei, Imaging anisotropic waveguide exciton polaritons in tin sulfide. *Nano Lett.* **22**, 1497–1503 (2022).
21. I. Soltero, J. Guerrero-Sánchez, F. Mireles, D. A. Ruiz-Tijerina, Moiré band structures of twisted phosphorene bilayers. *Phys. Rev. B* **105**, 235421 (2022).
22. J. Liu, X. Zhang, G. Lu, Non-adiabatic exciton dynamics in van der Waals heterostructures. *J. Phys. Chem. Lett.* **13**, 11760–11769 (2022).
23. X. Ling, L. Liang, S. Huang, A. A. Puretzky, D. B. Geohegan, B. G. Sumpter, J. Kong, V. Meunier, M. S. Dresselhaus, Low-frequency interlayer breathing modes in few-layer black phosphorus. *Nano Lett.* **15**, 4080–4088 (2015).
24. Y. Cai, Q. Ke, G. Zhang, Y. P. Feng, V. B. Shenoy, Y. W. Zhang, Giant phononic anisotropy and unusual anharmonicity of phosphorene: Interlayer coupling and strain engineering. *Adv. Funct. Mater.* **25**, 2230–2236 (2015).
25. A. Rossi, J. Zipfel, I. Maity, M. Lorenzon, L. Francaviglia, E. Regan, Z. Zhang, J. Nie, E. Barnard, K. Watanabe, "Anomalous interlayer exciton diffusion in WS2/WSe2 moiré heterostructure" (2023); https://doi.org/10.21203/rs.3.rs-2627775/v1.
26. J. P. Eisenstein, A. H. MacDonald, Bose–Einstein condensation of excitons in bilayer electron systems. *Nature* **432**, 691–694 (2004).
27. L. V. Butov, C. W. Lai, A. L. Ivanov, A. C. Gossard, D. S. Chemla, Towards Bose–Einstein condensation of excitons in potential traps. *Nature* **417**, 47–52 (2002).
28. M. M. Fogler, L. V. Butov, K. S. Novoselov, High-temperature superfluidity with indirect excitons in van der Waals heterostructures. *Nat. Commun.* **5**, 4555 (2014).
29. K. Ulman, S. Y. Quek, Organic-2D material heterostructures: A promising platform for exciton condensation and multiplication. *Nano Lett.* **21**, 8888–8894 (2021).
30. H. Guo, X. Zhang, G. Lu, Tuning moiré excitons in Janus heterobilayers for high-temperature Bose-Einstein condensation. *Sci. Adv.* **8**, eabp9757 (2022).
31. Z. Wang, D. A. Rhodes, K. Watanabe, T. Taniguchi, J. C. Hone, J. Shan, K. F. Mak, Evidence of high-temperature exciton condensation in two-dimensional atomic double layers. *Nature* **574**, 76–80 (2019).
32. T. Kinoshita, T. Wenger, D. S. Weiss, Observation of a one-dimensional Tonks-Girardeau gas. *Science* **305**, 1125–1128 (2004).
33. B. Paredes, A. Widera, V. Murg, O. Mandel, S. Fölling, I. Cirac, G. V. Shlyapnikov, T. W. Hänsch, I. Bloch, Tonks–Girardeau gas of ultracold atoms in an optical lattice. *Nature* **429**, 277–281 (2004).
34. D. Snoke, Spontaneous Bose coherence of excitons and polaritons. *Science* **298**, 1368–1372 (2002).
35. K. L. Seyler, P. Rivera, H. Yu, N. P. Wilson, E. L. Ray, D. G. Mandrus, J. Yan, W. Yao, X. Xu, Signatures of moiré-trapped valley excitons in $MoSe_2/WSe_2$ heterobilayers. *Nature* **567**, 66–70 (2019).
36. V. Bagnato, D. E. Pritchard, D. Kleppner, Bose-Einstein condensation in an external potential. *Phys. Rev. A* **35**, 4354–4358 (1987).
37. W. Ketterle, N. Van Druten, Bose-Einstein condensation of a finite number of particles trapped in one or three dimensions. *Phys. Rev. A* **54**, 656–660 (1996).
38. G. Kresse, J. Furthmüller, Efficient iterative schemes for ab initio total-energy calculations using a plane-wave basis set. *Phys. Rev. B Condens Matter* **54**, 11169–11186 (1996).
39. G. Kresse, J. Furthmüller, Efficiency of ab-initio total energy calculations for metals and semiconductors using a plane-wave basis set. *Comput. Mater. Sci.* **6**, 15–50 (1996).
40. J. P. Perdew, K. Burke, M. Ernzerhof, Generalized gradient approximation made simple. *Phys. Rev. Lett.* **77**, 3865–3868 (1996).
41. P. Blöchl, Projector augmented-wave method. *Phys. Rev. B* **50**, 17953–17979 (1994).
42. S. Grimme, Semiempirical GGA-type density functional constructed with a long-range dispersion correction. *J. Comput. Chem.* **27**, 1787–1799 (2006).
43. E. K. U. Gross, W. Kohn, Local density-functional theory of frequency-dependent linear response. *Phys. Rev. Lett.* **55**, 2850–2852 (1985).
44. M. A. Marques, N. T. Maitra, F. M. Nogueira, E. K. Gross, A. Rubio, *Fundamentals of Time-Dependent Density Functional Theory* (Springer Science & Business Media, 2012), vol. 837.
45. H. Guo, X. Zhang, G. Lu, Moiré excitons in defective van der Waals heterostructures. *Proc. Natl. Acad. Sci. U.S.A.* **118**, e2105468118 (2021).
46. L. Zhang, X. Zhang, G. Lu, One-dimensional flat bands and anisotropic moiré excitons in twisted tin sulfide bilayers. *Chem. Mater.* **33**, 7432–7440 (2021).
47. J. Liu, X. Zhang, G. Lu, Excitonic effect drives ultrafast dynamics in van der Waals heterostructures. *Nano Lett.* **20**, 4631–4637 (2020).
48. L.-y. Huang, X. Zhang, M. Zhang, G. Lu, Effect of point defects on optical properties of graphene fluoride: A first-principles study. *J. Phys. Chem. C* **121**, 12855–12862 (2017).
49. S. Refaely-Abramson, M. Jain, S. Sharifzadeh, J. B. Neaton, L. Kronik, Solid-state optical absorption from optimally tuned time-dependent range-separated hybrid density functional theory. *Phys. Rev. B* **92**, 081204 (2015).
50. S. Refaely-Abramson, S. Sharifzadeh, M. Jain, R. Baer, J. B. Neaton, L. Kronik, Gap renormalization of molecular crystals from density-functional theory. *Phys. Rev. B* **88**, 081204 (2013).
51. D. Wing, J. B. Haber, R. Noff, B. Barker, D. A. Egger, A. Ramasubramaniam, S. G. Louie, J. B. Neaton, L. Kronik, Comparing time-dependent density functional theory with many-body perturbation theory for semiconductors: Screened range-separated hybrids and the *GW* plus Bethe-Salpeter approach. *Phys. Rev. Mater.* **3**, 064603 (2019).
52. S. Refaely-Abramson, S. Sharifzadeh, N. Govind, J. Autschbach, J. B. Neaton, R. Baer, L. Kronik, Quasiparticle spectra from a nonempirical optimally tuned range-separated hybrid density functional. *Phys. Rev. Lett.* **109**, 226405 (2012).
53. L. Kronik, J. B. Neaton, Excited-state properties of molecular solids from first principles. *Ann. Rev. Phys. Chem.* **67**, 587–616 (2016).
54. J. Sun, C. A. Ullrich, Optical properties of $CsCu_2X_3$(X = Cl, Br, and I): A comparative study between hybrid time-dependent density-functional theory and the Bethe-Salpeter equation. *Phys. Rev. Mater.* **4**, 095402 (2020).
55. A. Tal, P. Liu, G. Kresse, A. Pasquarello, Accurate optical spectra through time-dependent density functional theory based on screening-dependent hybrid functionals. *Phys. Rev. Res.* **2**, 032019 (2020).
56. Z.-h. Yang, F. Sottile, C. A. Ullrich, Simple screened exact-exchange approach for excitonic properties in solids. *Phys. Rev. B* **92**, 035202 (2015).
57. M. E. Casida, *Recent Advances in Density Functional Methods*, D. P. Chong, Ed. (World Scientific, 1995), vol. 1.
58. X. Zhang, Z. Li, G. Lu, First-principles simulations of exciton diffusion in organic semiconductors. *Phys. Rev. B* **84**, 235208 (2011).
59. R. Tian, R. Fei, S. Hu, T. Li, B. Zheng, Y. Shi, J. Zhao, L. Zhang, X. Gan, X. Wang, Observation of excitonic series in monolayer and few-layer black phosphorus. *Phys. Rev. B* **101**, 235407 (2020).
60. H.-Y. Chen, V. A. Jhalani, M. Palummo, M. Bernardi, Ab initio calculations of exciton radiative lifetimes in bulk crystals, nanostructures, and molecules. *Phys. Rev. B* **100**, 075135 (2019).
61. J. C. Tully, Molecular dynamics with electronic transitions. *J. Chem. Phys.* **93**, 1061–1071 (1990).
62. W. R. Duncan, C. F. Craig, O. V. Prezhdo, Time-domain ab initio study of charge relaxation and recombination in dye-sensitized TiO_2. *J. Am. Chem. Soc.* **129**, 8528–8543 (2007).

Downloaded from https://www.science.org on December 19, 2025

63. S. A. Fischer, B. F. Habenicht, A. B. Madrid, W. R. Duncan, O. V. Prezhdo, Regarding the validity of the time-dependent Kohn–Sham approach for electron-nuclear dynamics via trajectory surface hopping. *J. Chem. Phys.* **134**, 024102 (2011).
64. H. Guo, W. Chu, O. V. Prezhdo, Q. Zheng, J. Zhao, Strong modulation of band gap, carrier mobility and lifetime in two-dimensional black phosphorene through acoustic phonon excitation. *J. Phys. Chem. Lett.* **12**, 3960–3967 (2021).
65. H. Guo, W. Chu, Q. Zheng, J. Zhao, Tuning the carrier lifetime in black phosphorene through family atom doping. *J. Phys. Chem. Lett.* **11**, 4662–4667 (2020).
66. Q. Zheng, W. Chu, C. Zhao, L. Zhang, H. Guo, Y. Wang, X. Jiang, J. Zhao, Ab initio non-adiabatic molecular dynamics investigations on the excited carriers in condensed matter systems. *WIREs Comput. Mol. Sci.* **9**, e1411 (2019).

Acknowledgments
Funding: This work was supported by the NSF-PREM program (DMR1828019) and the Army Research Office (W911NF-20-10305 and W911NF-23-10205). **Author contributions:** G.L. designed the study, and H.G. carried out calculations with the assistance of X.Z. G.L. supervised the research and wrote the manuscript with H.G. All authors discussed the results. **Competing interests:** The authors declare that they have no competing interests. **Data and materials availability:** All data needed to evaluate the conclusions in the paper are present in the paper and the Supplementary Materials.

Submitted 2 May 2023
Accepted 20 June 2023
Published 21 July 2023
10.1126/sciadv.adi5404

Downloaded from https://www.science.org on December 19, 2025